Journal of Computational Physics 227 (2008) 8699–8713

Contents lists available at ScienceDirect

Journal of Computational Physics

journal homepage: www.elsevier.com/locate/jcp

Multidimensional upwinding for incompressible flows based on characteristics

Kamiar Zamzamian [a,*], Seyed Esmail Razavi [b]

[a] Mechanical Engeering Department, Islamic Azad University, Tabriz Branch, Tabriz-Tehran Road, 2nd km, Tabriz 253587, Iran
[b] School of Mechanical Engineering, University of Tabriz, Tabriz, Iran

ARTICLE INFO

Article history:
Received 6 January 2008
Received in revised form 19 June 2008
Accepted 19 June 2008
Available online 28 June 2008

Keywords:
Incompressible flow
Artificial compressibility
Navier–Stokes equations
MCB scheme
Wave angle

ABSTRACT

In this paper, the multidimensional characteristic based upwind scheme (MCB) which has been recently introduced by the authors is applied to two another benchmark problems namely flow in a channel with a backward facing step and two-dimensional steady and unsteady flows past a circular cylinder. Extension of MCB scheme for calculating convective fluxes on non-Cartesian grids is presented here. For the flow over backward facing step, obtained results were compared against well-known experimental data and the results show high accuracy of MCB scheme and faster convergence rate with respect to conventional CB scheme. In the case of flow over circular cylinder, the flow at steady and transient regimes is investigated by MCB scheme. Again, the results obtained by MCB are compared to the other results in the literature and show good agreement with them. Also, rapid convergence rate of MCB was observed in this case too. It is concluded that, the genuinely multidimensional characteristic based (MCB) scheme, has been introduced earlier by the authors, is a robust and powerful scheme for modeling incompressible viscous flows for achieving the high accuracy and remarkable advantage in convergence rate with respect to conventional characteristic based schemes.

1. Introduction

Many numerical methods f or incompressible flows are predominantly based on the pressure correction schemes. The artificial compressibility method of Chorin [1] can be considered as an alternative among others. In this method, a pseudo-time derivative of pressure is added to the continuity equation, thus turning the system of governing equations into hyperbolic ones and it is possible to use time-marching methods for obtaining steady state solutions. In time-marching, the addition of artificial compressibility has no effect on the steady state results. However, it may affect the convergence process [2]. In pseudo-time marching, the numerical waves created are used for propagating information throughout the solution domain and driving the divergence of velocity to zero. Different numerical schemes have been used for discretization of artificial compressibility equations. Among them, Farmer et al. have used a central scheme with Jameson's artificial viscosity to prevent the pressure–velocity decoupling [3]. The discretization schemes and solvers developed for artificial compressibility have many similarities with the methods of compressible flows. Many researchers used Godunov-type schemes to discretize the equations of artificial compressibility. Rogers et al. [4], Liu et al. [5], Kallinderis et al. [6], and Yuan [7] used Roe's flux difference splitting for solution of incompressible flow fields. Their Roe's averaging approach was applied to artificial compressibility equations and obtained fluxes in finite-volume discretization are functions of artificial compressibility parameter. Traditionally, the method of characteristics is used primarily for compressible flow calculations. By introducing the pseudo-time

* Corresponding author. Tel.: +98 914 3165385.
E-mail address: k_zamzamian@yahoo.com (K. Zamzamian).

0021-9991/$ - see front matter © 2008 Elsevier Inc. All rights reserved.
doi:10.1016/j.jcp.2008.06.018

derivative in Chorin's formulation, it is possible that the incompressible flow equations be solved by a similar method of characteristics. For the first time Drikakis et al. used one-dimensional characteristic relations to calculate the convective fluxes in finite-volume discretization for two-dimensional incompressible flow in a curvilinear coordinate system on structured grids [8]. The method was developed for three-dimensional flows [9] and further developed to incorporate multigrid techniques [10]. This method was extended by Zhao et al. for simulation of incompressible flows and convection heat transfer on unstructured two- and three-dimensional grids [11–15]. Flow variables are calculated along characteristics paths in the direction normal to the surface of a control volume and their initial values are interpolated based on the signs of the corresponding characteristic speeds. The CB scheme has been used for a broad range of incompressible flow simulations. Siong et al. used an implicit finite-volume CB method for calculating incompressible flow in porous media on unstructured grids [16]. Drikakis and Shapiro applied the artificial compressibility method for solving flows with various densities by using a locally one-dimensional characteristic scheme [17,18]. Other case studies of CB schemes in conjunction with artificial compressibility for modeling incompressible flow can be found in Refs. [19–23].

In all of the examples in the literature, the characteristic based schemes for artificial compressibility equations are constructed under the assumption of locally one-dimensional flow in certain directions. All extensions of characteristic based upwind schemes to two and three dimensions ignore the multidimensional nature of flow and advance the solution by "splitting" that is to say, through a sequence of one-dimensional operators. For example, the CB scheme which is mentioned above, exhibits substantial delays in terms of convergence in certain studies [23–25] without obeying the real physical nature of flow because using one-dimensional characteristic relations. To take into account the real multidimensional nature of flow, it is necessary to devise methods which consider the actual directions in which information is propagated. Different ideas have been proposed for the definition of multidimensional upwind schemes for compressible Euler equations whereas in the case of incompressible flows, the first genuinely multidimensional characteristic based scheme has been introduced by the authors recently [26]. The idea was tested in [26] for the cavity flow on a pure Cartesian grid and MCB showed very good behaviour against CB and central schemes. In this paper, the MCB is extended for non-Cartesian grids and the solution of two benchmark problems including flow in a channel with a backward facing step and two-dimensional steady and unsteady flows past a circular cylinder are presented using it.

2. Governing equations

The Navier–Stokes equations for two-dimensional incompressible flows modified by the artificial compressibility can be expressed as

$$\iint_{Vol.} \frac{\partial \mathbf{W}}{\partial t}\,dV + \oint_C (\mathbf{F}\,dy - \mathbf{G}\,dx) = \oint_C (\mathbf{R}\,dy - \mathbf{S}\,dx), \tag{1}$$

where

$$\mathbf{W} = \begin{bmatrix} p \\ u \\ v \end{bmatrix}, \quad \mathbf{F} = \begin{bmatrix} \beta u \\ u^2 + p \\ uv \end{bmatrix}, \quad \mathbf{G} = \begin{bmatrix} \beta v \\ uv \\ v^2 + p \end{bmatrix},$$
$$\mathbf{R} = \frac{1}{Re}\begin{bmatrix} 0 \\ \partial u/\partial x \\ \partial v/\partial x \end{bmatrix}, \quad \mathbf{S} = \frac{1}{Re}\begin{bmatrix} 0 \\ \partial u/\partial y \\ \partial v/\partial y \end{bmatrix}.$$

Here, **W** is the vector of primitive variables, **F**, **G** and **R**, **S** are convective and viscous flux vectors, respectively. The artificial compressibility parameter and Reynolds number are shown by β and *Re, respectively. The above equations have been non-dimensionalized based on the following scalings:*

$$\begin{aligned} &(x, y) = (x^*/l^*, y^*/l^*), \quad t = \frac{t^*}{l^*/U_{\mathrm{ref}}}, \\ &(u, v) = (u^*/U_{\mathrm{ref}}, v^*/U_{\mathrm{ref}}), \quad p = \frac{p^* - p_{\mathrm{ref}}}{\rho_{\mathrm{ref}} U_{\mathrm{ref}}^2}. \end{aligned} \tag{2}$$

The discretized form of Eq. (1) reads

$$A_{ij}\frac{\partial \mathbf{W}_{ij}}{\partial t} + \sum_{k=1}^{4}(\mathbf{F}\Delta y - \mathbf{G}\Delta x)_k = \sum_{k=1}^{4}(\mathbf{R}\Delta y - \mathbf{S}\Delta x)_k, \tag{3}$$

where A_{ij} is the cell area.

3. Characteristic structure for two-dimensional incompressible flows

Derivation of mathematical relations for characteristic structure of incompressible flows corrected by artificial compressibility concept, has been presented in [26] for the first time by the authors.

To derive the characteristic relations of incompressible flows, their corresponding "Euler equations" are considered [11]. These equations modified by artificial compressibility for deriving two-dimensional characteristic structures are

$$\begin{cases} \frac{\partial p}{\partial t} + \beta \frac{\partial u}{\partial x} + \beta \frac{\partial v}{\partial y} = 0, \\ \frac{\partial u}{\partial t} + u \frac{\partial u}{\partial x} + v \frac{\partial u}{\partial y} + \frac{\partial p}{\partial x} = 0, \\ \frac{\partial v}{\partial t} + u \frac{\partial v}{\partial x} + v \frac{\partial v}{\partial y} + \frac{\partial p}{\partial y} = 0. \end{cases} \tag{4}$$

To obtain characteristic structure of equations, a characteristic surface in the form of $f(x, y, t) = 0$ is assumed. Using the kinematics relations for relating the partial derivatives to exact derivatives corresponding to the assumed surface, one gets the following system of equations [27,28]:

$$\begin{bmatrix} f_t/\beta & f_x & f_y \\ f_x & \psi & 0 \\ f_y & 0 & \psi \end{bmatrix} \begin{bmatrix} \mathrm{d}p \\ \mathrm{d}u \\ \mathrm{d}v \end{bmatrix} = \begin{bmatrix} 0 \\ 0 \\ 0 \end{bmatrix}, \tag{5}$$

where the subscripts stand for the partial differentiation and ψ is defined as

$$\psi = \frac{\partial f}{\partial t} + u \frac{\partial f}{\partial x} + v \frac{\partial f}{\partial y}. \tag{6}$$

For compatibility requirements of Eq. (5), the determinant of coefficient matrix is set to zero, hence,

$$\psi = 0, \quad \psi = \frac{\beta}{f_t}(f_x^2 + f_y^2). \tag{7}$$

We assumed the pseudo-velocity vector $\hat{V} = (u, v, 1)$ and normal vector to characteristic surface $\hat{n} = (\cos\varphi, \sin\varphi, n_t)$ alike compressible Euler equations [29], in which φ shows the wave direction. Expressing Eqs. (7) in terms of vectors $\hat{V}$ and $\hat{n}$, two types of characteristic surface corresponding to following relations are obtained:

$$\begin{cases} \hat{V} \cdot \hat{n} = 0, \\ \hat{V} \cdot \hat{n} = \frac{\beta}{n_t}, \end{cases} \tag{8}$$

where $n_t = f_t/\sqrt{f_x^2 + f_y^2}$ denotes the t-component of normal vector. By some mathematical operations, n_t takes the following forms:

$$n_t = \frac{-(u\cos\varphi + v\sin\varphi) \pm \sqrt{(u\cos\varphi + v\sin\varphi)^2 + 4\beta}}{2} = n_1, n_2. \tag{9}$$

Regarding the dual roots of second relation at Eq. (8) as a function of n_t, similar to compressible Euler equations, dual characteristic surfaces would exist. With straightforward mathematical operations it can be proven that the roots have always different signs. This depicts the growth of zones of influence and dependence around the pseudo-streamlines. The projection of normal vectors n_t in the x–y plane lies inside a unit circle (Fig. 1). Two roots of Eq. (9) for n_t denote the biplanes tangent to characteristic surfaces passing through a certain point and producing the Mach cones. Also, Mach conoid is tangent to Mach cone at each point passing through it. Along bicharacteristics, the characteristic surfaces are tangent to passing Mach cone. In fact, the characteristic paths corresponding to the first equation of (8) demonstrate the pseudo-pathlines and the second one

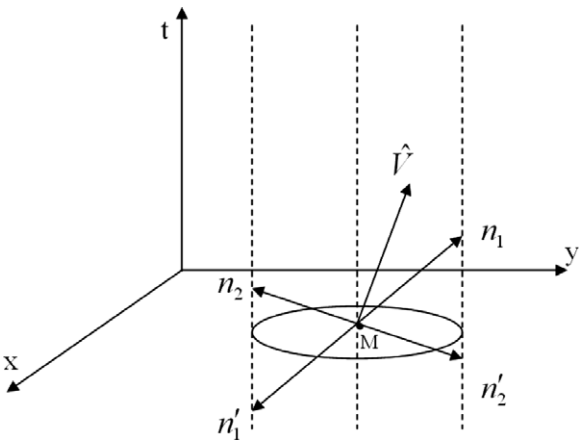

Fig. 1. Envelope of normal vectors to characteristic surfaces.

corresponds to the pseudo-acoustic waves propagating within the incompressible flow field. To specify the wave paths on a Mach conoid, consider an assumed characteristic path on $f(x,y,t)=0$. Taking $\mathrm{d}f/\mathrm{d}t=0$ yields

$$\frac{\partial f}{\partial t}+\frac{\mathrm{d}x}{\mathrm{d}t}\frac{\partial f}{\partial x}+\frac{\mathrm{d}y}{\mathrm{d}t}\frac{\partial f}{\partial y}=0. \tag{10}$$

From Eq. (10) one gets

$$n_t+(\mathrm{d}x/\mathrm{d}t)\cos\varphi+(\mathrm{d}y/\mathrm{d}t)\sin\varphi=0. \tag{11}$$

To obtain the equations of characteristic paths on the Mach cone (virtual acoustic waves), the above equation and the second relation of Eqs. (8) (indicator of pseudo-acoustic wave fronts) are combined as

$$\begin{cases} n_t+(\mathrm{d}x/\mathrm{d}t)\cos\varphi+(\mathrm{d}y/\mathrm{d}t)\sin\varphi=0, \\ n_t+u\cos\varphi+v\sin\varphi=\beta/n_t. \end{cases} \tag{12}$$

Combining the above relations with each other results in the following:

$$(u-\mathrm{d}x/\mathrm{d}t)\cos\varphi+(v-\mathrm{d}y/\mathrm{d}t)\sin\varphi=\beta/n_t. \tag{13}$$

By the aid of Eq. (13) and considering the fact that planes tangent to characteristic surfaces form the Mach cone, the generators of this cone are (similar to compressible flow case such as [28])

$$\begin{cases} \frac{\mathrm{d}x}{\mathrm{d}t}=u-\frac{\beta}{n_t}\cos\varphi, \\ \frac{\mathrm{d}y}{\mathrm{d}t}=v-\frac{\beta}{n_t}\sin\varphi, \end{cases} \tag{14}$$

where φ is wave angle. By considering Eq. (9), it is concluded that similar to compressible Euler equations, dual characteristic surfaces would exist, so that their corresponding tangential planes construct two Mach cones which extend from a certain point, namely domain of dependence and domain of influence (Fig. 2). Similar approaches for two-dimensional characteristic structure of compressible Euler equations have been presented at Refs. [29–32].

As it is seen in Fig. 2, for any angle in the range $0\leqslant\varphi\leqslant2\pi$ there exist two bicharacteristics. Unlike compressible Euler equations, here the cross-section of Mach cone with x–y plane produce an ellipse (called Mach ellipse) having minor and major axes parallel to the coordinate axes. The compatibility relations corresponding to pseudo-acoustic waves are obtained from Eq. (5) by taking the second value of ψ from Eqs. (7), as

$$\begin{cases} \frac{\beta}{n_t}\mathrm{d}u+\cos\varphi\,\mathrm{d}p=0, \\ \frac{\beta}{n_t}\mathrm{d}v+\sin\varphi\,\mathrm{d}p=0. \end{cases} \tag{15}$$

Eqs. (15) are valid for both $n_t=n_1,n_2$ which shows the governing compatibility relations along bicharacteristics.

4. Conventional CB scheme

The conventional CB scheme with second-order interpolation has been used in this paper for comparing with the new proposed scheme. In this section, second-order CB scheme relations which have been used here are presented. It should

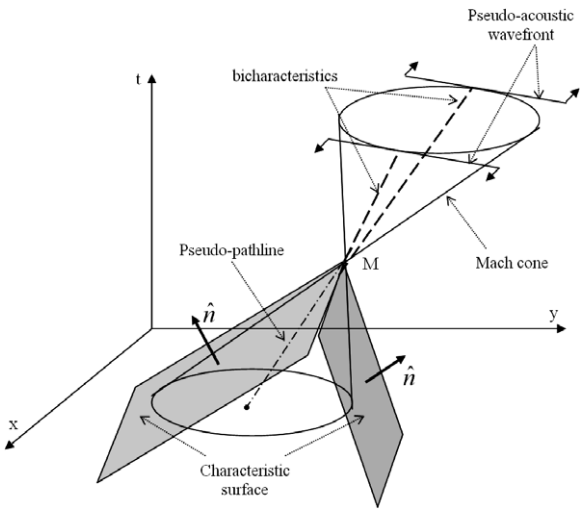

Fig. 2. Characteristic structure for incompressible flow defined by artificial compressibility equations.

be noted that these relations are based on presented CB scheme in the literature such as [8,11–15]. If (n_x, n_y, n_z) denotes the unit normal vector to common face of two cells, the relations for determining flow quantities on the common face is as follows [11–15]:

$$\begin{cases} u = fn_x + u^0 n_y^2 - v^0 n_x n_y, \\ v = fn_y + v^0 n_x^2 - u^0 n_y n_x, \\ p = p^1 - \lambda^1[(u-u^1)n_x + (v-v^1)n_y], \end{cases} \tag{16}$$

where

$$\begin{aligned} \lambda^0 &= un_x + vn_y, \\ \lambda^1 &= \lambda^0 + C, \\ \lambda^2 &= \lambda^0 - C, \\ C &= \sqrt{(\lambda^0)^2 + \beta}, \\ f &= \frac{1}{2C}[(p^1 - p^2) + n_x(\lambda^1 u^1 - \lambda^2 u^2) + n_y(\lambda^1 v^1 - \lambda^2 v^2)]. \end{aligned} \tag{17}$$

Flow quantities at new time level obtained from the above equations on the locally one-dimensional characteristics are used to calculate fluxes at the common face of two cells. The quantities at the prior time level are evaluated by upwind method using the sign of characteristics as follows:

$$\phi^j = \frac{1}{2}[(1 + \mathrm{sign}(\lambda^j))\phi_L + (1 - \mathrm{sign}(\lambda^j))\phi_R], \tag{18}$$

in which ϕ is the typical name for flow quantities.

For second-order interpolation in this paper, following relations have been used:

$$\begin{aligned} \phi_L &= \phi_i + 0.25\phi_{i+1} - 0.25\phi_{i-1}, \\ \phi_R &= \phi_{i+1} + 0.25\phi_i - 0.25\phi_{i+2}. \end{aligned} \tag{19}$$

5. Proposed numerical scheme

Proposed MCB scheme in [26] has been devised only for Cartesian grids by selection of four pseudo-acoustic waves. In this paper, by using the same selection of four acoustic waves, the relations for calculation of convective fluxes on a general grid is presented and the scheme is extended to non-Cartesian grids. By selection of four pseudo-acoustic waves aligned to grid and by the aid of their corresponding compatibility relations, all of the cell interface values from previous time level are estimated. The viscous fluxes are computed with conventional averaging method.

5.1. Convective fluxes

To evaluate the convective fluxes, four pseudo-acoustic waves with the projected propagation paths normal and parallel to the cell interface are selected. According to Fig. 3, the intersection of local Mach cone corresponding to point M, on the two cells interfaces, with x–y plane, demonstrates the real two-dimensional nature of information propagation; we called it "Mach ellipse". As it is seen in Fig. 4, to take into account the physical behaviour of domain of influence for point M (or face * in Figs. 3 and 4), four pseudo-waves corresponding to grid directions are selected and Eqs. (15) are discretized along them.

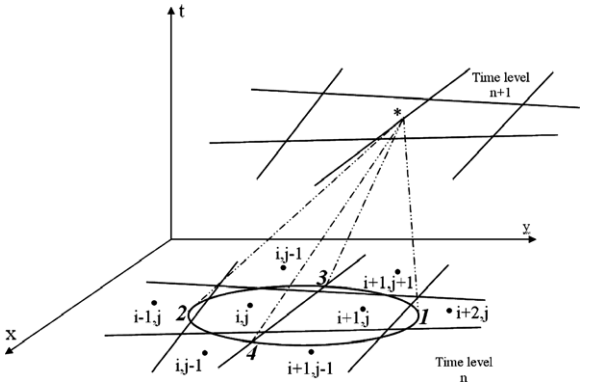

Fig. 3. Intersection of local Mach cone with previous time plane which produces "Mach ellipse".

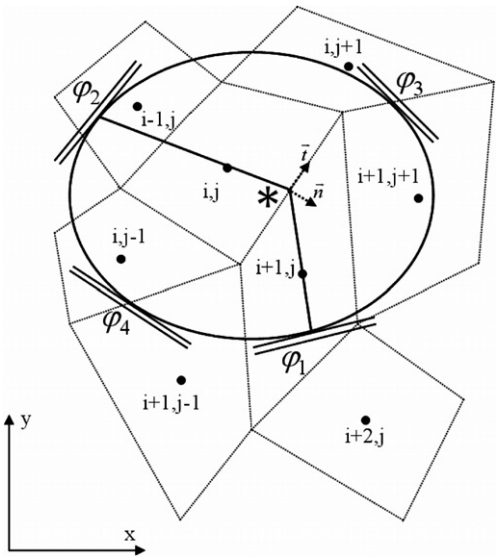

Fig. 4. MCB stencil for evaluating convective fluxes.

It should be noted that in Fig. 4, φ for any wave is the angle between x-axis and normal vector to presented directions corresponding to φ_1–φ_4. In order to evaluate the convective flux at face * in Fig. 4, two φ_1, φ_2 pseudo-acoustic waves corresponding to n direction and two φ_3, φ_4 waves corresponding to t direction are selected. In which n is the normal vector to common face between (i,j) and $(i+1,j)$ and t is normal to n (Fig. 4). This is an alternative, such as done for compressible wave models introduced by Roe and others [33–35]. It is possible to select different numbers and directions for waves and use their corresponding compatibility relations for evaluating interface values. The method of selection of waves in this paper is explained below.

For face * of Fig. 4, for choosing φ_1, the intersection of the line between midpoint of face * and the center of cell $(i+1,j)$ with Mach ellipse is considered. The value of φ_1 is determined by the tangent to Mach ellipse at this point. For wave φ_2 this procedure is repeated by using cell (i,j) in stead of $(i+1,j)$. The wave angle φ_3 is considered at the intersection of Mach ellipse with the common face of cells $(i,j+1)$ and $(i+1,j+1)$. Similarly, φ_4 is chosen at the intersection of Mach ellipse with the face in common between cells $(i,j-1)$ and $(i+1,j-1)$.

By using Eq. (15), four compatibility equations corresponding to φ_1, φ_2 are obtained as following:

$$\begin{cases} \frac{\beta}{n_{t1}}\,du + \cos\varphi_1\,dp = 0, & x\text{-direction compatibility relation of } \varphi_1 \text{ wave;} \\ \frac{\beta}{n_{t1}}\,dv + \sin\varphi_1\,dp = 0, & y\text{-direction compatibility relation of } \varphi_1 \text{ wave;} \\ \frac{\beta}{n_{t2}}\,du + \cos\varphi_2\,dp = 0, & x\text{-direction compatibility relation of } \varphi_2 \text{ wave;} \\ \frac{\beta}{n_{t2}}\,dv + \sin\varphi_2\,dp = 0, & y\text{-direction compatibility relation of } \varphi_2 \text{ wave;} \end{cases} \tag{20}$$

where n_{t1} and n_{t2} obtained from Eq. (9) with respect to wave angles φ_1 or φ_2. It should be noted that in Eqs. (20), n_t with positive sign (from Eq. (9)) is used. Similar to Eqs. (20), one can write four compatibility relations corresponding to waves φ_3 and φ_4. Discretizing Eqs. (20) along their corresponding paths, results in the following relations:

$$\begin{cases} p^* - p_1 + A(u^* - u_1) = 0, \\ p^* - p_1 + B(v^* - v_1) = 0, \\ p^* - p_2 + C(u^* - u_2) = 0, \\ p^* - p_2 + D(v^* - v_2) = 0, \end{cases} \tag{21}$$

where A, B, C, D can be obtained from Eqs. (9) and (20) as following:

$$\begin{cases} A = 2\beta/\left\{\cos\varphi_1[-u_1\cos\varphi_1 - v_1\sin\varphi_1 + \sqrt{(u_1\cos\varphi_1 + v_1\sin\varphi_1)^2 + 4\beta}]\right\}, \\ B = 2\beta/\left\{\sin\varphi_1[-u_1\cos\varphi_1 - v_1\sin\varphi_1 + \sqrt{(u_1\cos\varphi_1 + v_1\sin\varphi_1)^2 + 4\beta}]\right\}, \\ C = 2\beta/\left\{\cos\varphi_2[-u_2\cos\varphi_2 - v_2\sin\varphi_2 + \sqrt{(u_2\cos\varphi_2 + v_2\sin\varphi_2)^2 + 4\beta}]\right\}, \\ D = 2\beta/\left\{\sin\varphi_2[-u_2\cos\varphi_2 - v_2\sin\varphi_2 + \sqrt{(u_2\cos\varphi_2 + v_2\sin\varphi_2)^2 + 4\beta}]\right\}. \end{cases} \tag{22}$$

It should be noted that four similar relations can be written for the wave angles φ_3 and φ_4. In Eqs. (21), p^*, u^* and v^* denote the flow variables at cell interface. At first, u^* and p^* are calculated from the first and third equations of Eqs. (21). The v^* and p^* are determined using second and fourth equations. Two values of p^* is then averaged and considered as final value. It should be said that each equation includes flow information which is transported from time n to time $n+1$, and any of them cannot be neglected.

The calculated values for u^* and v^* from Eqs. (21) are projected on direction n and similarly the obtained values from corresponding φ_3 and φ_4 compatibility relations are projected on direction t in order to calculate the velocity components on the cell interface (Fig. 4). Averaging values of obtained pressure from compatibility relations is considered as pressure value on the cell interfaces. This procedure is explained below in detail.

Let us assume that $u^*_{1,2}, v^*_{1,2}$ and $p^*_{1,2}$ are the calculated values from Eqs. (21) corresponding to φ_1, φ_2 as explained above and $u^*_{3,4}, v^*_{3,4}$ and $p^*_{3,4}$ are those corresponding to φ_3, φ_4 waves similarly. Now, as mentioned above, we project the vector $(u^*_{1,2}, v^*_{1,2})$ on direction n (Fig. 4) and call it $\vec{V}_n$ and similarly the projected vector $(u^*_{3,4}, v^*_{3,4})$ on direction t is called $\vec{V}_t$. Then, the final velocity vector at two cells interface $(\vec{V^*})$ can be defined as $\vec{V^*} = \vec{V}_n + \vec{V}_t$ and the final value of pressure at interface (p^*) is taken as $p^* = \frac{1}{2}(p^*_{1,2} + p^*_{3,4})$.

The star values are computed from eight compatibility relations (corresponding to four pseudo-acoustic waves) with respect to flow properties at points 1–4 (Figs. 3 and 4) in the previous time level for an explicit time integration. With this idea, a genuinely multidimensional upwind scheme, called MCB (multidimensional characteristic based), has been developed for evaluation of fluxes at the cell interfaces. In the first-order MCB scheme, flow properties at points 1, 2 are set to neighborhood cell values and for points 3, 4 interpolated from two cells containing assumed face. For second-order MCB scheme, the values of point 1 interpolated from cells $(i+1,j)$ and $(i+2,j)$ and similarly for point 2 interpolated from cells (i,j) and $(i-1,j)$. Flow properties at point 3 are interpolated from cells $(i,j+1)$ and $(i+1,j+1)$ and also for point 4 is done similarly.

5.2. Viscous fluxes

To evaluate the viscous fluxes, one needs to compute flow variables derivatives at the cell interfaces as it is shown in Fig. 5. For example, the first-order derivative at the side AB in Fig. 5 is determined using the secondary cell ANBM as follows:

$$\begin{aligned}\left.\frac{\partial\phi}{\partial x}\right|_{AB} &= \frac{1}{S'}\iint_{S'}\frac{\partial\phi}{\partial x}\,dS = \frac{1}{S'}\oint_{\partial S'}\phi\,dy = \frac{1}{S'}\sum_{k=1}^{4}\phi_k\Delta y_k,\\ &= \frac{1}{S'}[0.5(\phi_N+\phi_A)\Delta y_{AN} + 0.5(\phi_N+\phi_B)\Delta y_{NB} + 0.5(\phi_B+\phi_M)\Delta y_{BM} + 0.5(\phi_M+\phi_A)\Delta y_{MA}],\end{aligned} \tag{23}$$

where S' denotes the area of AMBN. Also the ϕ_A and ϕ_B are found by averaging from the neighboring cells. Here, ϕ is a generic name standing for the flow variables.

5.3. Time integration

The spatially discretized equations form a set of coupled ordinary differential equations which are integrated in time by an explicit fourth-order Runge–Kutta scheme. The discretized equations are in the following form:

$$\frac{\partial W}{\partial t} + \mathbf{Q} = 0. \tag{24}$$

After time discretization one gets

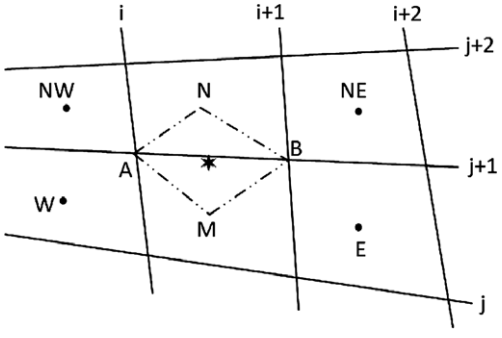

Fig. 5. Pattern for discretization of viscous terms.

$$\mathbf{W}^{(0)} = \mathbf{W}^{(n)}, \quad \mathbf{W}^{(1)} = \mathbf{W}^{(0)} - \frac{\Delta t}{2}\mathbf{Q}^{(0)};$$
$$\mathbf{W}^{(2)} = \mathbf{W}^{(0)} - \frac{\Delta t}{2}\mathbf{Q}^{(1)}, \quad \mathbf{W}^{(3)} = \mathbf{W}^{(0)} - \Delta t\mathbf{Q}^{(2)}; \tag{25}$$
$$\mathbf{W}^{(4)} = \mathbf{W}^{(0)} - \frac{\Delta t}{6}(\mathbf{Q}^{(0)} + 2\mathbf{Q}^{(1)} + 2\mathbf{Q}^{(2)} + \mathbf{Q}^{(3)});$$

where $\mathbf{Q}$ contains the convective and viscous terms. The maximum time step is determined from

$$\mathrm{CFL} = [\sqrt{u^2 + v^2} + \sqrt{u^2 + v^2 + \beta}]\frac{\Delta t}{\Delta l}. \tag{26}$$

Here, Δl is taken as the smallest distance between any cell center with its neighbor cell center.

6. Results and discussion

Extension of proposed MCB scheme in [26] to non-Cartesian grids has been performed here and two well-known benchmark problems including flow in a channel with a backward facing step and two-dimensional steady and unsteady flows past a circular cylinder are simulated to show its ability and robustness. Incompressible flow in a channel with a backward facing step is an example with grids which clustered inherently at vertical direction (non-Cartesian). In the case of flow past a circular cylinder, an O mesh has been used which is also non-Cartesian and in addition the ability of MCB scheme in unsteady flow simulations has been tested by calculating the flow field at $Re > 40$.

6.1. Incompressible flow in channel with a backward facing step

In this section, the flow over a backward facing step has been investigated using second-order MCB scheme. In this case, the grid is clustered inherently at *x-direction. According to experimental results of Denham and Patrick [36], we have performed computations for a backward facing step with inlet to channel expansion ratio 2:3 at* $Re = 73$ and $Re = 229$. The Reynolds number is defined based on the step height and average velocity at the inlet profile. For $Re = 73$, the downstream channel length is considered as 30 step heights and for $Re = 229$ it is equal to 60 step heights. Applied boundary conditions on solid walls are no-slip condition and normal momentum equation for pressure calculation. At inlet boundary, the velocity components are set by inlet velocity profile values while interpolating the pressure. At outlet boundary, the pressure is fixed and velocity components are extrapolated. It should be noted that for $Re = 73$ the parabolic velocity profile at channel inlet is applied while for $Re = 229$ the experimental inlet profile differs significantly from the parabolic one and for this case, inlet boundary condition is generated by fitting a curve using the experimental inlet data [36].

Results obtained for u-velocity profile at some sections using second-order CB [8], second-order MCB and central scheme with artificial dissipation in comparison with experimental results of Denham and Patrick [36] are shown in Fig. 6 for the case of $Re = 73$ ($x = 0$ is the section of channel on the step). The computations have been performed on a grid containing 9×24 nodes in the inlet section and 81×36 nodes in the main channel. As it is shown in Fig. 6, results obtained by second-order MCB and central scheme approximately have the same accuracy while for second-order CB scheme significant deviation from experimental data is observed. In Fig. 7 comparison of obtained results using second-order MCB and CB schemes with respect to experimental data for $Re = 229$ is presented for some sections of channel. For this case, a grid containing 8×30 nodes in the inlet section and 112×45 nodes in the main channel has been used. The downstream channel length is considered as 60 step heights. It should be noted that for this case, the central scheme shows remarkable instabilities and comparisons are made only for second-order MCB and CB schemes. As it is

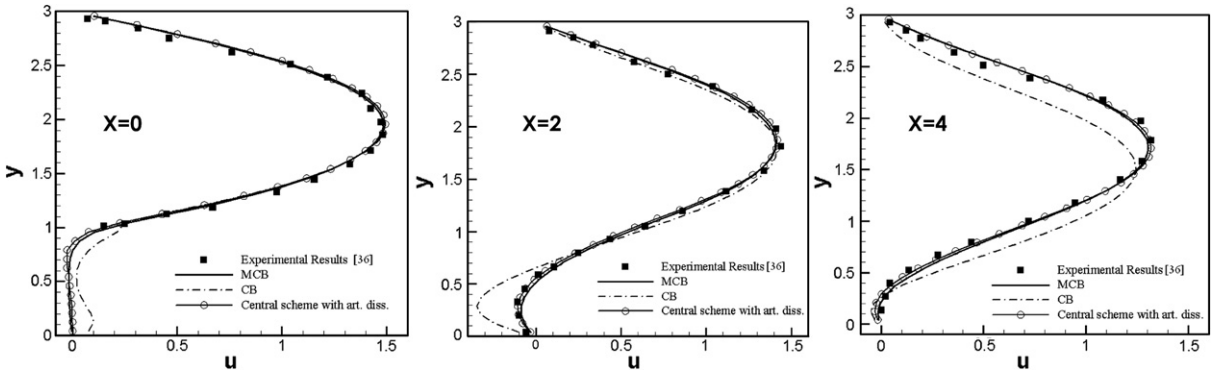

Fig. 6. Comparison of results for u-velocity profile at some sections obtained by the central, second-order CB and second-order MCB schemes at $Re = 73$.

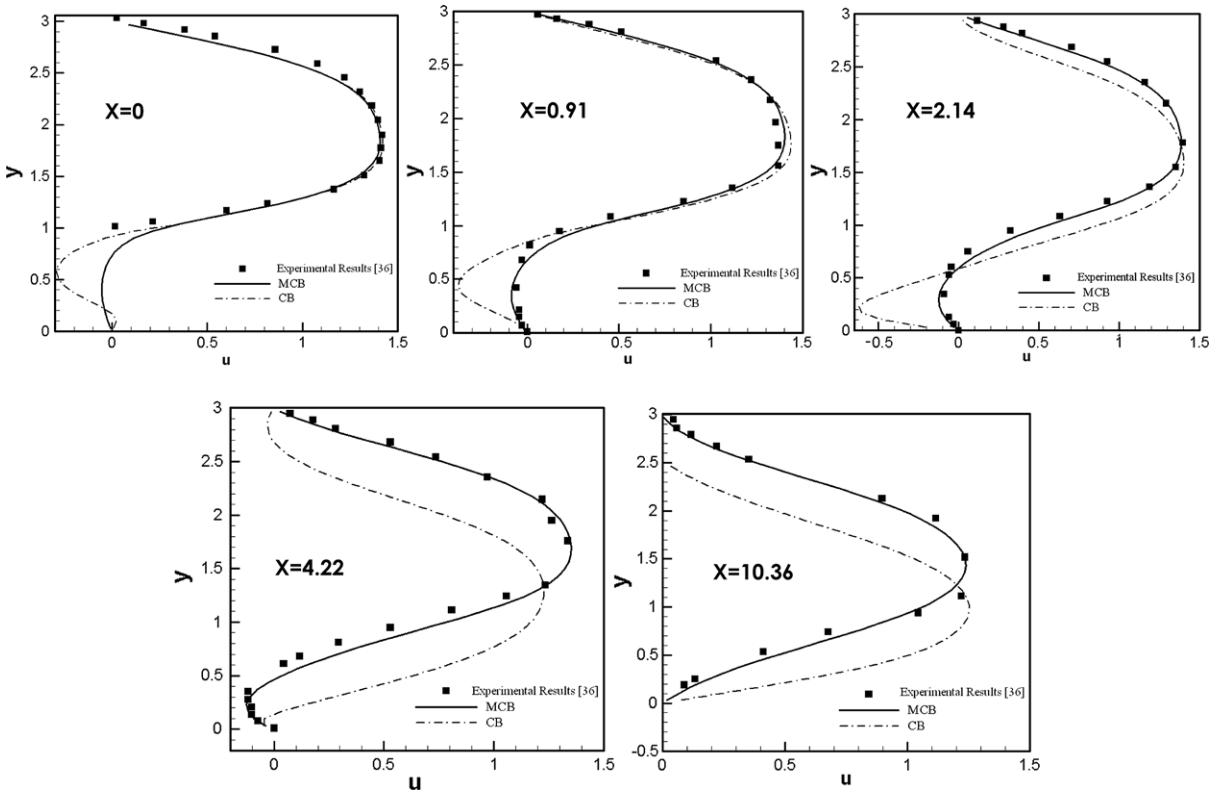

Fig. 7. Comparison of results for u-velocity profile at some sections obtained by second-order CB and MCB schemes at *Re* = 229.

observed in Fig. 7, second-order MCB provides more accurate results than second-order CB scheme on the same grid in this case.

Convergence rates of three mentioned schemes have been tested for various grid size and typical cases of them are shown in Figs. 8 and 9 for *Re* = 73 and *Re* = 229. In Fig. 8, convergence rates for three schemes are presented for *Re* = 73 at two different grids. Considered grids are a grid containing 9×24 nodes in the inlet section and 81×36 nodes in the main channel and another one contains 12×36 nodes in inlet section and 108×54 nodes in main channel. For *Re* = 229, the comparison between second-order CB and MCB schemes in terms of convergence is presented at Fig. 9 for a grid containing 8×30 nodes in the inlet section and 112×45 nodes in the main channel. It should be noted that in this case, the downstream channel

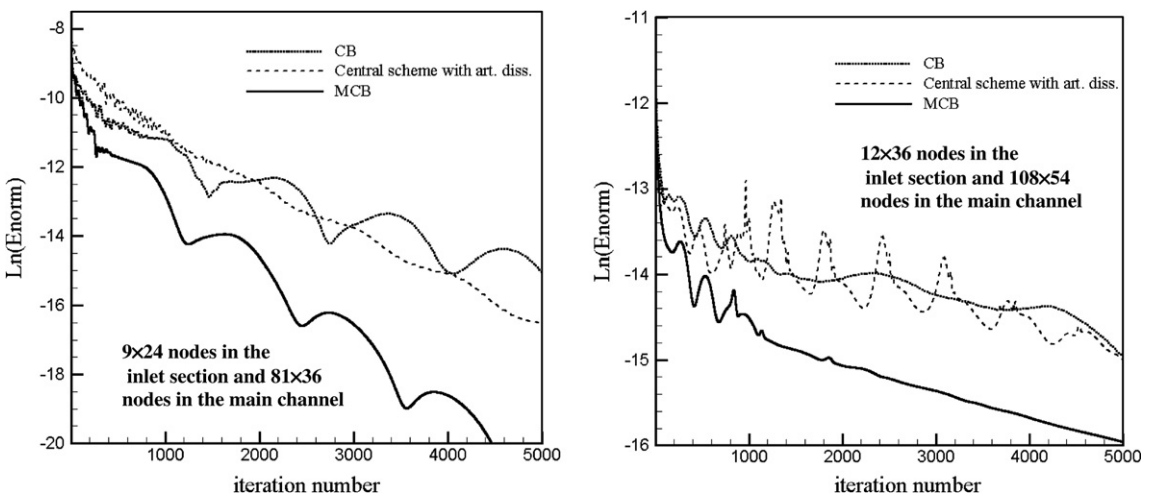

Fig. 8. Comparison of convergence histories for three studied schemes for backward step problem at *Re* = 73 for the two types of grid size.

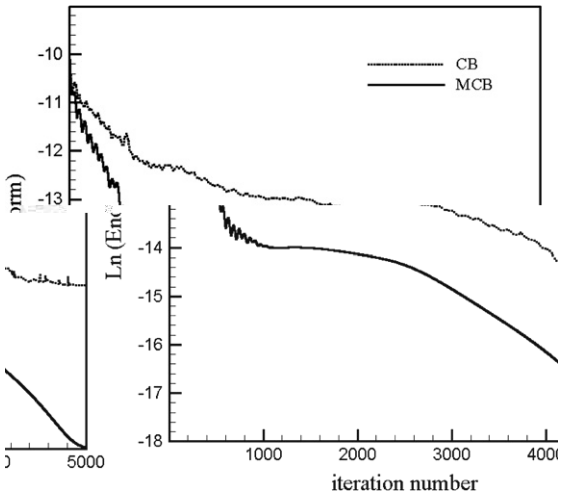

Fig. 9. Comparison of convergence histories for second-order CB and MCB schemes for backward step problem at $Re = 229$ and a grid containing 8×30 nodes in the inlet section and 112×45 nodes in the main channel.

length is considered as 60 step heights. By considering Figs. 8 and 9 superiority of MCB scheme in the case of convergence behaviour in the backward facing step test case is obvious.

Fig. 10 shows streamlines for $Re = 73$ and 229 obtained by second-order MCB scheme. For comparing the results of MCB with experimental data of Denham and Patrick [36] in details, solution of fine grid is presented in Fig. 11. Grids used in this case are a grid containing 18×90 nodes in the inlet section and 162×135 nodes in the main channel for $Re = 73$ and a grid containing 24×90 nodes in the inlet section and 336×135 nodes in the main channel for $Re = 229$.

6.2. Incompressible flow past a circular cylinder

To verify the ability of MCB scheme on non-Cartesian grids, incompressible steady and unsteady flow past a circular cylinder is considered here along with an O grid clustered near solid wall (Fig. 12). The Reynolds number is defined based on the free stream uniform inlet velocity and the cylinder diameter. At an inlet boundary, the velocity components are set to free-stream values while interpolating the pressure. At an outlet boundary, the pressure is fixed and velocity components are extrapolated.

6.2.1. Steady flow past a circular cylinder

The first case is incompressible flow past a circular cylinder in steady regime in which $Re \leqslant 40$. Fig. 13 presents the results obtained by the second-order MCB scheme in comparison with conventional second-order CB [8] and central schemes for wall spanwise vorticity along the cylinder surface at $Re = 40$ on 80×80 grid. As it is seen, the second-order MCB scheme again provides more accurate results in this case. The convergence rate of three mentioned schemes is studied at different low Reynolds numbers and the MCB scheme shows remarkable reduction and distinction in all of them. As a typical case, convergence rates are presented in Fig. 14 for $Re = 40$ on 80×80 grid. Table 1 provides the comparison of drag coefficient predicted by MCB at different Reynolds numbers. As it is observed, the results are in good agreement with the other reported

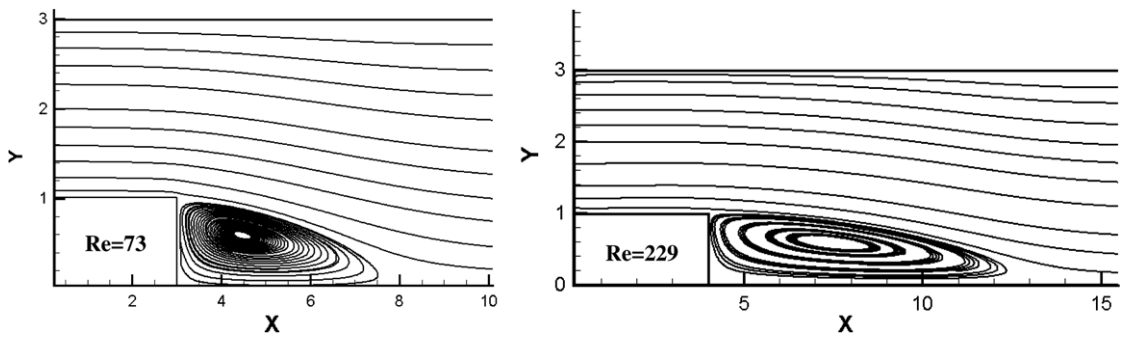

Fig. 10. Streamlines of separated flow near the expansion at $Re = 73$ and 229.

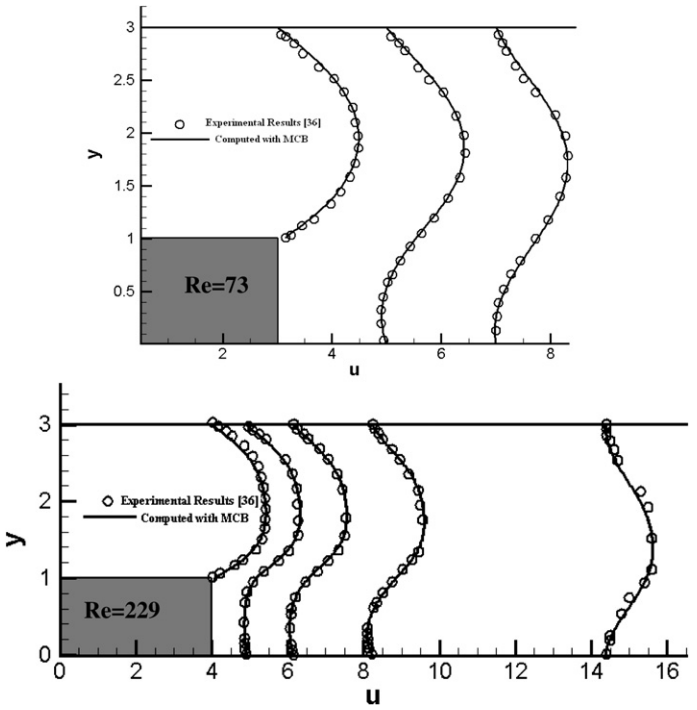

Fig. 11. Comparison of obtained velocity distributions with experimental data [36] for $Re = 73$ and 229.

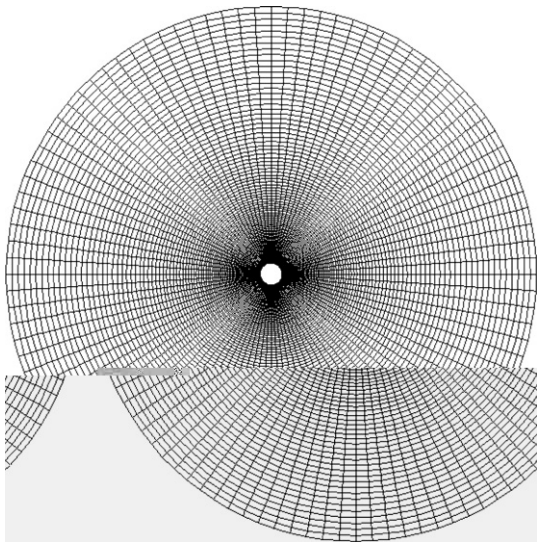

Fig. 12. O shape grid by clustering near the solid wall.

solutions. It is shown in Fig. 15 that the pressure coefficient at $Re = 40$ obtained using MCB scheme agrees well with that of Choi et al. [37].

6.2.2. Transient flow past a circular cylinder

In this section, the results obtained from the second-order MCB scheme for transient incompressible flow past a circular cylinder are presented. Fig. 16 shows unsteady streamlines variations at different times for $Re = 100$. As it is seen, the present method clearly captures vortex shedding behind the cylinder. In Fig. 17 variation of drag coefficient versus Reynolds number in the unsteady flow regime is shown comparing to the other results in the literature. Fig. 18 shows instantaneous pressure and velocity components contours at $Re = 100$.

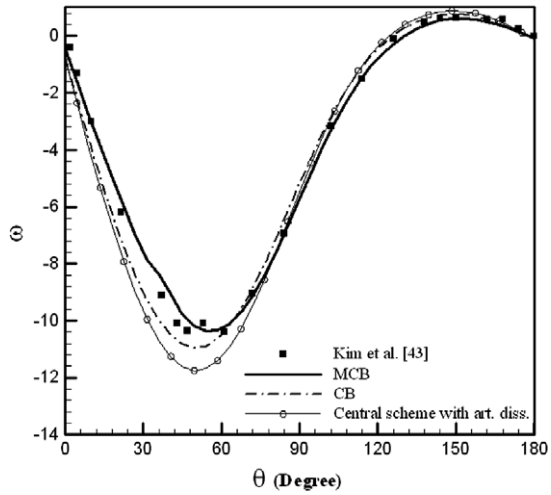

Fig. 13. Comparison of obtained results for wall spanwise vorticity along the cylinder surface, $Re = 40$ and 80×80 grid. (see above-mentioned references for further information.)

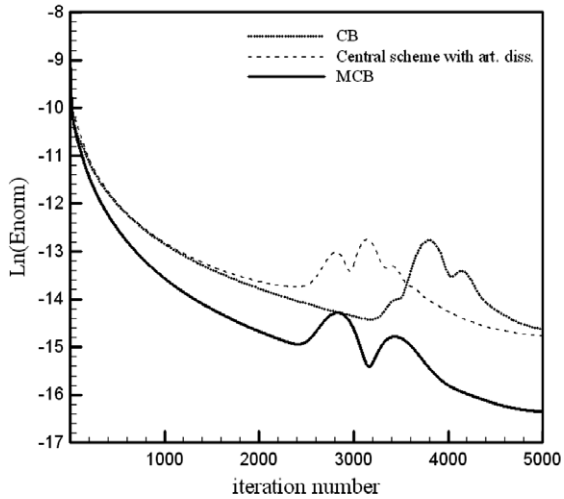

Fig. 14. Comparison of convergence histories for the flow past a circular cylinder, $Re = 40$ and 80×80 grid.

Table 1
Comparison of mean drag coefficient for laminar steady flow past a circular cylinder at low Reynolds numbers

Re	References	Drag coefficient
10	Dennis and Chang [38]	2.85
	Takami and Keller [39]	2.80
	Tuann and Olson [40]	3.18
	Ding et al. [41]	3.07
	Nithiarasu et al. [42]	2.85
	Present (MCB result)	2.98
20	Dennis and Chang [38]	2.05
	Takami and Keller [39]	2.01
	Tuann and Olson [40]	2.25
	Ding et al. [41]	2.18
	Nithiarasu et al. [42]	2.06
	Present (MCB result)	2.03
40	Dennis and Chang [38]	1.522
	Takami and Keller [39]	1.536
	Tuann and Olson [40]	1.675
	Ding et al. [41]	1.713
	Nithiarasu et al. [42]	1.564
	Present (MCB result)	1.55

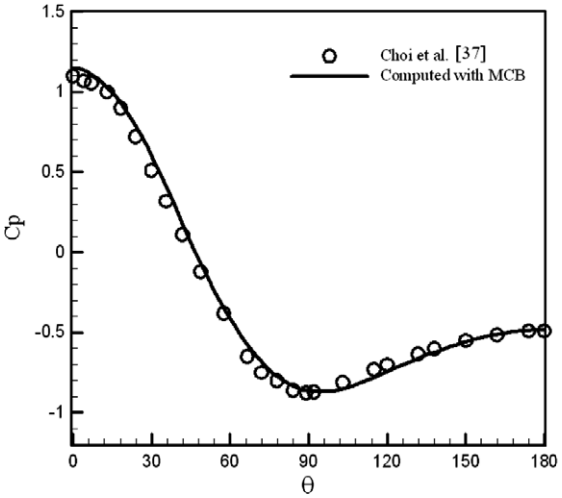

Fig. 15. Comparison of wall pressure coefficient along the cylinder surface at $Re = 40$ with Choi et al. [37].

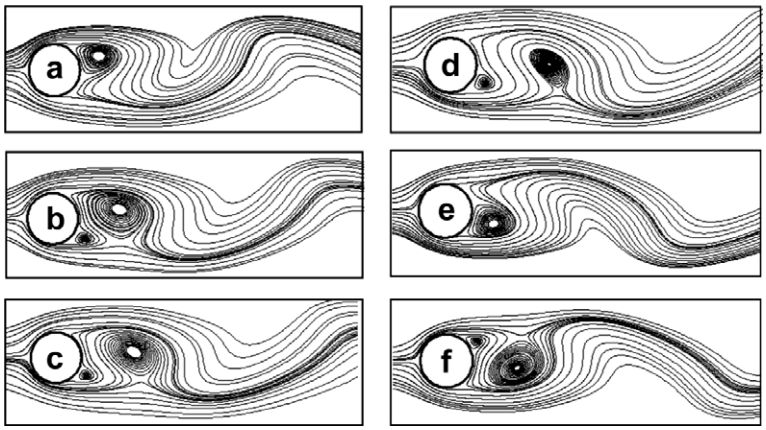

Fig. 16. Unsteady streamlines at different times for $Re = 100$.

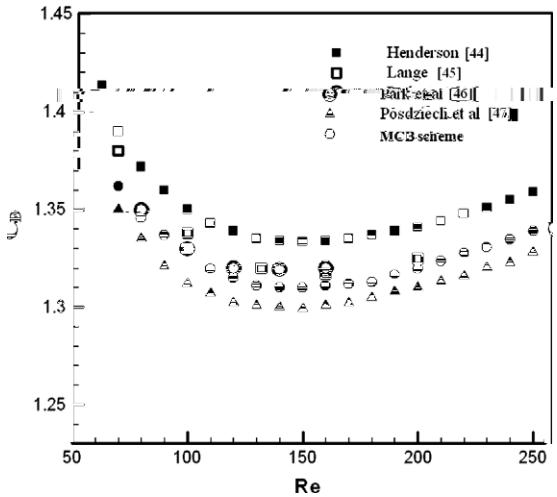

Fig. 17. Variation of drag coefficient versus Reynolds number. (see above-mentioned references for further information.)

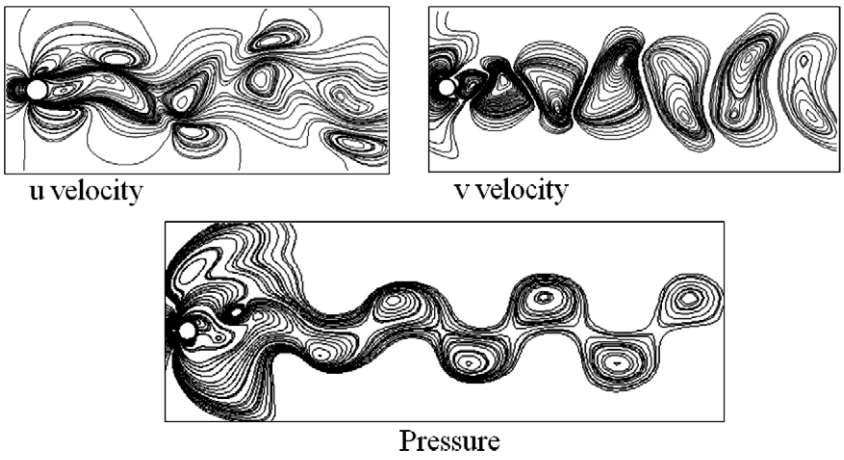

Fig. 18. Instantaneous pressure and velocity contours at $Re = 100$.

7. Conclusions

Recently proposed genuinely multidimensional characteristic based upwind scheme for incompressible flows (MCB) by authors has been extended in this paper for non-Cartesian grids and applied to other case studies. The original version of MCB scheme was implemented to Cartesian grids and has been tested only for cavity flow. By using this idea, an algorithm for calculation of convective fluxes by MCB scheme on general meshes was presented in this paper. By selecting four acoustic waves, the relations for calculation of convective fluxes on a general grid were presented and the scheme was extended to non-Cartesian grids. By selection of four pseudo-acoustic waves aligned to grid and by the aid of their corresponding compatibility relations, all of the cell interface values from previous time level can be estimated. Two well-known benchmark problems including flow in a channel with a backward facing step and two-dimensional steady and unsteady flows past a circular cylinder were used as test cases. For the flow over backward facing step, obtained results were compared against well-known experimental data and the results show high accuracy of second-order MCB scheme and faster convergence rate. In the case of flow over circular cylinder, the flow at steady and transient regimes is investigated by MCB scheme. Again, the results obtained by second-order MCB are compared to the other results in the literature and show good agreement with them. The remarkable advantage of MCB scheme lies in fast convergence rate with respect to other studied schemes, noting the slow convergence of CB reported in the literature. Another advantage of MCB is its stable solutions and also there is no need to add artificial viscosity even at high Reynolds numbers due to its inherent upwinding and characteristic based nature. It is concluded that, the genuinely multidimensional characteristic based (MCB) scheme, is robust and powerful for modeling incompressible viscous flows for achieving the high accuracy and remarkable advantage in convergence rate with respect to conventional characteristic based schemes.

References

[1] A.J. Chorin, A numerical method for solving incompressible viscous flow problems, Journal of Computational Physics 2 (1967) 12–26.
[2] D. Kwak, C. Kiris, C.S. Kim, Computational challenges of viscous incompressible flows, Computers and Fluids 34 (2005) 283–299.
[3] J. Farmer, L. Martinelli, A. Jameson, Fast multigrid method for solving incompressible hydrodynamic problems with free surface, AIAA Journal 32 (1994) 1175–1182.
[4] S.E. Rogers, D. Kwak, Steady and unsteady solutions of the incompressible Navier–Stokes equations, AIAA Journal 29 (1991) 603–610.
[5] C. Liu, X. Zheng, C.H. Sung, Preconditioned multigrid methods for unsteady incompressible flows, Journal of Computational Physics 139 (1998) 35–57.
[6] Y. Kallinderis, H.T. Ahn, Incompressible Navier–Stokes method with general hybrid meshes, Journal of Computational Physics 210 (2005) 75–108.
[7] L. Yuan, Comparison of implicit multigrid schemes for three-dimensional incompressible flows, Journal of Computational Physics 177 (2002) 134–155.
[8] D. Drikakis, P.A. Govatsos, D.E. Papantonis, A characteristic based method for incompressible flows, International Journal for Numerical Methods in Fluids 19 (1994) 667–685.
[9] D. Drikakis, A parallel multiblock characteristic based method for three-dimensional incompressible flows, Advances in Engineering Software 26 (1996) 111–119.
[10] D. Drikakis, O.P. Iliev, D.P. Vassileva, A nonlinear multigrid method for the three-dimensional incompressible Navier–Stokes equations, Journal of Computational Physics 146 (1998) 301–321.
[11] Y. Zhao, B. Zhang, A high-order characteristics upwind FV method for incompressible flow and heat transfer simulation on unstructured grids, Computer Methods in Applied Mechanics and Engineering 190 (2000) 733–756.
[12] C.H. Tai, Y. Zhao, Parallel unsteady incompressible viscous flow computations using an unstructured multigrid method, Journal of Computational Physics 192 (2003) 277–311.
[13] C.H. Tai, Y. Zhao, K.M. Liew, Parallel computation of unsteady three-dimensional incompressible viscous flow using an unstructured multigrid method, Computers and Structures 82 (2004) 2425–2436.
[14] C.H. Tai, Y. Zhao, K.M. Liew, Parallel-multigrid computation of unsteady incompressible viscous flows using a matrix-free implicit method and high-resolution characteristics-based scheme, Computer Methods in Applied Mechanics and Engineering 194 (2005) 3949–3983.
[15] C.H. Tai, Y. Zhao, K.M. Liew, Parallel computation of unsteady incompressible viscous flows around moving rigid bodies using an immersed object method with overlapping grids, Journal of Computational Physics 207 (2005) 151–172.

[16] K. Siong, C.Y. Zhao, Numerical study of steady/unsteady flow and heat transfer in porous media using a characteristics-based matrix-free implicit FV method on unstructured grids, International Journal of Heat and Fluid Flow 25 (2004) 1015–1033.
[17] E. Shapiro, D. Drikakis, Artificial compressibility, characteristics-based schemes for variable density, incompressible, multi-species flows. Part I. Derivation of different formulations and constant density limit, Journal of Computational Physics 210 (2005) 584–607.
[18] E. Shapiro, D. Drikakis, Artificial compressibility, characteristics-based schemes for variable density, incompressible, multi-species flows. Part II. Multigrid implementation and numerical tests, Journal of Computational Physics 210 (2005) 608–631.
[19] D. Drikakis, U. Goldberg, Wall-distance-free turbulence models applied to incompressible flows, International Journal of Computational Fluid Dynamics 10 (1998) 241–253.
[20] F. Mallinger, D. Drikakis, Instability in three-dimensional unsteady stenotic flows, International Journal of Computational Heat Fluid Flow 23 (2002) 657–663.
[21] D. Drikakis, P.K. Smolarkiewicz, On spurious vortical structures, Journal of Computational Physics 172 (2001) 309–325.
[22] D. Drikakis, Bifurcation phenomena in incompressible sudden expansion flows, Physics of Fluids 9 (1997) 76–87.
[23] P. Neofytou, D. Drikakis, Non-Newtonian flow instability in a channel with a sudden expansion, Journal of Non-Newtonian Fluid Mechanics 111 (2003) 127–150.
[24] P. Neofytou, D. Drikakis, M.A. Leschziner, Study of Newtonian and non Newtonian fluid flow in a channel with a moving indentation, in: Sajjadi, S., Nash, G., Rampling, M. (Eds.), Proceedings of the IMA Conference on Cardiovascular Flow Modelling with Application to Clinical Medicine, Salford, UK, 1998, Clarendon Press, Oxford, 1999.
[25] P. Neofytou, Revision of the characteristics-based scheme for incompressible flows, Journal of Computational Physics 222 (2007) 475–484.
[26] S.E. Razavi, K. Zamzamian, A. Farzadi, Genuinely multidimensional characteristic-based scheme for incompressible flows, International Journal for Numerical Methods in Fluids 57 (2008) 929–949.
[27] S.E. Razavi, Far field boundary conditions for computation of compressible aerodynamic flows, Ph.D. thesis, Department of Mechanical Engineering, McGill University, Montreal, Canada, 1995.
[28] L. Fox, Numerical Solution of Ordinary and Partial Differential Equations, Pergamon Press, Oxford, 1962.
[29] M.J. Zacrow, J.D. Hoffman, Gas Dynamics, vol. 2, John Wiley and Sons, New York, 1976.
[30] C. Osnaghi, Explicit evaluation of discontinuities in 2D unsteady flows solved by the method of characteristics, in: 11th International Conference on Numerical Methods in Fluid Dynamics, Lecture Notes in Physics, No. 323, 1988.
[31] L. Zannetti, G. Colasurdo, Unsteady compressible flow: a computational method consistent with the physical phenomena, AIAA Journal 19 (1981) 852–856.
[32] L. Zannetti, G. Moretti, Numerical experiments on the leading-edge flowfield, AIAA Journal 20 (12) (1981).
[33] P.L. Roe, Discrete models for the numerical analysis of time dependent multidimensional gas dynamics, Journal of Computational Physics 63 (2) (1986) 458–476.
[34] H. Paillere, H. Deconinck, R. Struijs, P.L. Roe, L.M. Measaros, J.D. Muller, Computations of inviscid compressible flows using fluctuation splitting on triangular meshes, AIAA-93-3301-CP, 1993.
[35] C. Rumsey, B. Van Leer, P.L. Roe, Effect of a multi-dimensional flux function on the monotonicity of Euler and Navier–Stokes computations, AIAA-91-4530-CP, 1991.
[36] M.K. Denham, M.A. Patrik, Laminar flow over a downstream-facing step in a two-dimensional flow channel, Transactions of the Institution of Chemical Engineers 52 (1974) 361–367.
[37] J. Choi, R.C. Oberoi, J.R. Edwards, J.A. Rosati, An immersed boundary method for complex incompressible flows, Journal of Computational Physics 224 (2007) 757–784.
[38] S.C.R. Dennis, G.Z. Chang, Numerical solutions for steady flow past a circular cylinder at Reynolds number up to 100, Journal of Fluid Mechanics (1970) 471–489.
[39] H. Takami, H.B. Keller, Steady two-dimensional viscous flow of an incompressible fluid past a circular cylinder, Physics of Fluids (Suppl. II-51) (1969).
[40] S.Y. Tuann, M.D. Olson, Numerical studies of the flow around a circular cylinder by a finite element method, Computers and Fluids (1978) 219–231.
[41] H. Ding, C. Shu, K.S. Yeo, D. Xu, Simulation of incompressible viscous flow past a circular cylinder by hybrid FD scheme and meshless least-square based finite difference method, Computer Methods in Applied Mechanics and Engineering 193 (2004) 727–744.
[42] P. Nithiarasu, O.C. Zienkiewicz, Analysis of an explicit and matrix free fractional step method for incompressible flows, Computer Methods in Applied Mechanics and Engineering 195 (2006) 5537–5551.